A semi-infinite bubble advancing into a planar tapered channel

D. Halpern and O. E. Jensen

Citation: Phys. Fluids **14**, 431 (2002); doi: 10.1063/1.1426393
View online: http://dx.doi.org/10.1063/1.1426393
View Table of Contents: http://pof.aip.org/resource/1/PHFLE6/v14/i2
Published by the American Institute of Physics.

ARTICLES

A semi-infinite bubble advancing into a planar tapered channel

D. Halpern
Department of Mathematics, University of Alabama, Tuscaloosa, Alabama 35487

O. E. Jensen
Division of Applied Mathematics, School of Mathematical Sciences, University of Nottingham, University Park, Nottingham NG7 2RD, United Kingdom

(Received 18 July 2001; accepted 16 October 2001)

We consider two problems in which a semi-infinite bubble moves into a uniformly convergent two-dimensional channel under creeping-flow conditions. In the first (steady) problem, the bubble is stationary with respect to the channel walls, which move away from the channel vertex parallel to themselves, each entraining a liquid film of uniform thickness; the appropriate flux is provided by a line source at the channel vertex. In the second (unsteady) problem, the channel walls are fixed and the bubble is drawn at a constant speed towards the channel vertex by a line sink. In this case the bubble interface assumes a self-similar shape, and wedge-shaped films are deposited on the channel walls. The boundary-element method, supported by asymptotic approximations, is used to compute flows over a range of bubble speeds (measured by a capillary number Ca) and wedge angles α. In the steady problem, the deposited film thickness increases monotonically with α at low Ca, but diminishes with increasing α at sufficiently high Ca. In the unsteady problem, the film thickness was found always to increase with both α and Ca. In both cases, the dimensionless pressure drop across the bubble tip can be nonmonotonic in α. Implications of these results in modeling coating and peeling flows are discussed. © *2002 American Institute of Physics.* [DOI: 10.1063/1.1426393]

I. INTRODUCTION

The problem of a semi-infinite bubble advancing into a uniform planar channel at zero Reynolds number, treated originally by Bretherton[1] and investigated subsequently by numerous workers,[2–7] has widespread application to coating flows,[8,9] two-phase flows in porous media[10] and certain topics in physiological fluid dynamics.[11,12] In the absence of inertia, the problem is parametrized by a single dimensionless quantity, the capillary number Ca, which measures the relative importance of viscous to capillary forces. As the bubble advances, a film is deposited on each channel wall, with faster-moving bubbles depositing thicker films. Bretherton showed how the film thickness can be predicted explicitly when $\mathrm{Ca} \ll 1$ using lubrication theory; for $\mathrm{Ca} \geqslant 0.01$, however, the film thickness must be determined by finding the complete flow numerically.

Many applications, such as roll coating[8,13] or the peeling apart of wet membranes,[14] involve the motion of a bubble in a channel of nonuniform width. Provided the channel width varies sufficiently slowly with distance, the ''Bretherton'' problem (at arbitrary Ca) emerges naturally as an ''inner'' asymptotic problem at the tip of the advancing meniscus.[2,15] Matching the Bretherton problem to the surrounding outer problems requires knowledge of the deposited film thickness and the net pressure drop across the bubble tip, each as functions of Ca. If the channel width varies too rapidly with distance, however, then the effects of wall taper in the inner problem are significant, and existing predictions of film thickness and pressure drop are inadequate. Channel taper is an important consideration in roll coating, where it can have a stabilizing effect on the critical value of Ca at which fingering instabilities develop.[16–18] In the human microcirculation, red blood cells can deform significantly as they squeeze through small blood vessels with an irregular cross-section; the gap between the red blood cell membrane and the capillary wall can be very small but the angle of inclination that the gap makes with the vessel axis may be significant, requiring changes to the standard lubrication theory equations.[19] Similarly, taper is an important factor limiting the accuracy of current asymptotic models of peeling processes. In particular, in work that motivated the present study,[20] in which we treated the propagation of a semi-infinite bubble into a liquid-filled, flexible-walled channel (a simple physical model for the reopening of an initially liquid-filled lung airway),[12] it is shown how the effects of channel taper on the Bretherton problem can have a direct bearing on the pressure required to peel open a collapsed lung airway.

In order to investigate the influence of channel taper on the thickness of the film deposited behind an advancing bubble, and on the net pressure drop across the bubble tip, we consider here two model problems in which a semi-infinite bubble advances into a planar, uniformly tapered converging channel. In the first problem (described in Sec. II), a bubble is at rest in a wedge-shaped channel, the walls

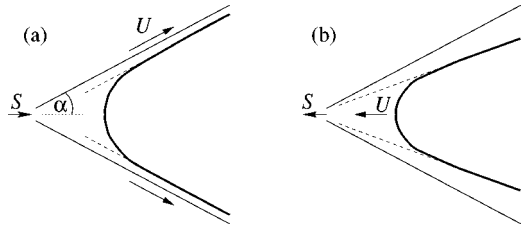

FIG. 1. A semi-infinite bubble in a planar, tapered channel, driven by a source or sink *S*. In (a) the bubble is stationary, the channel walls move outwards parallel to themselves; in (b) the walls are fixed and bubble advances steadily towards the vertex maintaining a self-similar shape.

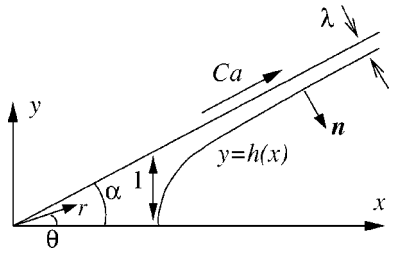

FIG. 2. Coordinates and variables for steady bubble motion.

of which move outwards parallel to themselves [Fig. 1(a)], each entraining a film that has uniform thickness far from the bubble tip. In the second problem (see Sec. III), a bubble is drawn into a tapered channel having fixed walls by a sink at the channel's vertex [Fig. 1(b)]; here the bubble assumes a self-similar shape as it moves steadily into the vertex, depositing wedge-shaped films on the channel walls far from the vertex. In each problem, the boundary-element method is used to solve the Stokes equations and to determine the interfacial shape. Numerical predictions of the deposited film thickness and pressure drop are checked against approximations valid for small wedge angle α or small Ca. Taper is shown to have unexpected and differing effects in the two problems. Implications of the results are discussed in Sec. IV.

II. A STATIONARY BUBBLE IN A TAPERED CHANNEL

A. The model

Consider the steady motion of a semi-infinite bubble which displaces fluid of viscosity μ in a wedge subtending an angle 2α at its vertex, as shown in Fig. 1(a). We assume symmetry about the midplane of the channel. The motion is driven by a line source placed at the vertex of the wedge and by the motion of the walls, which move parallel to themselves and away from the vertex with steady speed U. The source strength is chosen so that the bubble interface remains stationary. Let a be the vertical channel half-width at the bubble tip, so the bubble tip lies a distance $a\ \cot\alpha$ from the vertex. A film is swept onto the channel walls, having uniform thickness λa far from the bubble tip.

Taking γ to be the uniform surface tension at the bubble interface, we scale lengths on a, speeds on γ/μ, pressure on γ/a, and take the pressure in the bubble to be zero. The problem is then parametrized by the wedge angle α and the capillary number $\mathrm{Ca}=\mu U/\gamma$. Neglecting the effects of inertia, the flow is governed by the dimensionless continuity and Stokes equations,

$$0=\nabla\cdot\mathbf{u},\quad \mathbf{0}=-\nabla p+\nabla^2\mathbf{u}, \tag{1}$$

where $\mathbf{u}$ and p are the dimensionless velocity field and pressure, respectively. We introduce dimensionless Cartesian coordinates (x,y), so that the wall lies at $y=x\ \tan\alpha$ in $x>0$, the bubble tip at $(\cot\alpha,0)$, and the bubble interface at $y=h(x)$ for $x\geqslant\cot\alpha$ where $h(\cot\alpha)=0$, as shown in Fig. 2. Sufficiently far from the bubble tip, close to the vertex, the flow is described by a local solution given in Sec. II B below.

On the bubble interface, which has unit normal $\mathbf{n}$ and curvature κ, the stress boundary condition and kinematic condition are

$$\boldsymbol{\tau}\equiv\boldsymbol{\sigma}\cdot\mathbf{n}=\kappa\mathbf{n},\quad \mathbf{u}\cdot\mathbf{n}=0, \tag{2}$$

where $\boldsymbol{\tau}$ is the stress vector on the interface and $\boldsymbol{\sigma}=-\mathrm{I}p+\nabla\mathbf{u}+\nabla\mathbf{u}^T$ is the stress tensor. Symmetry about $y=0$ requires that for $0<x\leqslant\cot\alpha$,

$$u_y(x,0)=0,\ v(x,0)=0. \tag{3}$$

On the wall $y=x\ \tan\alpha$,

$$\mathbf{u}=\mathrm{Ca}(\cos\alpha,\sin\alpha). \tag{4}$$

The deposited film thickness $\lambda(\mathrm{Ca},\alpha)$, which must be determined as part of the solution, dictates the value of the volume flux,

$$\int_h^{x\ \tan\alpha} u\,dy=\lambda\ \mathrm{Ca}, \tag{5}$$

which must be uniform through the flow domain (where for convenience we define $h\equiv 0$ in $0<x<\cot\alpha$).

B. The flow near the vertex

To compute the flow near the vertex driven by the combined effects of the moving wall and the source, we introduce a streamfunction $\psi(r,\theta)$ dependent on polar coordinates (r,θ) (see Fig. 2), so that $\mathbf{u}=(\psi_\theta/r)\hat{\mathbf{r}}-\psi_r\hat{\boldsymbol{\theta}}$. Given (1), ψ satisfies the biharmonic equation,

$$\nabla^4\psi=0. \tag{6}$$

Exploiting the linearity of (6) and the boundary conditions (3), (4), we let $\psi=\psi_1+\psi_2$, where ψ_1 and ψ_2 describe, respectively, the flow due to the motion of the walls and the flow due to the source at the vertex. Let $\psi_1=rg_1(\theta)$ and $\psi_2=g_2(\theta)$, where [from (6)] g_1 and g_2 are solutions of

$$g_1'''+2g_1''+g_1=0,\quad g_2'''+4g_2''=0.$$

The boundary conditions on the flow driven by the moving wall are [from (4)] $g_1'(\alpha)=\mathrm{Ca}$, $g_1(\alpha)=0$, and [from (3)] $g_1(0)=g_1''(0)=0$; this flow has zero net flux. For the purely radial source flow (a low-Reynolds-number Jeffery–Hamel flow), (4) implies $g_2'(\alpha)=0$, and symmetry demands that $g_2(0)=g_2''(0)=0$. Thus

$$g_1(\theta)=\mathrm{Ca}\,\frac{\theta\ \cos\theta\ \sin\alpha-\alpha\ \cos\alpha\ \sin\theta}{\sin\alpha\ \cos\alpha-\alpha}, \tag{7a}$$

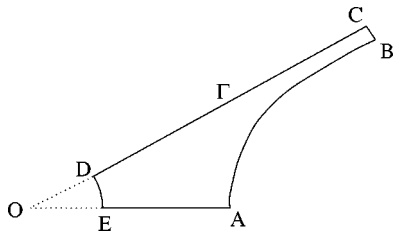

FIG. 3. The computational domain.

$$g_2(\theta)=S\frac{\sin 2\theta-2\theta\cos 2\alpha}{\sin 2\alpha-2\alpha\cos 2\alpha}, \tag{7b}$$

where $2S=2g_2(\alpha)$ is the strength of the source. By mass conservation (5), S is related to the deposited film thickness by $S=\lambda$ Ca, indicating that a source is necessary to balance the flux of fluid carried off beyond the bubble tip. The streamfunction near the vertex also has contributions that are self-similar solutions of the corresponding homogeneous problem.[21,22] For the range of wedge angles investigated here, however, these are significantly smaller than the two inhomogeneous solutions given in (7) for sufficiently small r. The structure of the near-vertex flow in the limit $\alpha\to 0$ is described in Sec. II E below.

The pressure near the vertex is

$$p\approx p_1(r,\theta)+p_2(r,\theta)+p_k,\quad p_1=-\frac{g_1'''+g_1'}{r},$$

$$p_2=-\frac{g_2'''}{2r^2}, \tag{8}$$

where $p_k(\mathrm{Ca},\alpha)$ is a constant contribution to the pressure set by the flow away from the vertex and the condition that the bubble pressure is zero. Below we shall compute what we call the net pressure drop across the bubble tip, which we define as the (negative) vertex pressure distribution (8) extrapolated to the bubble tip,

$$\Delta p=-[p_1(\cot\alpha,0)+p_2(\cot\alpha,0)+p_k]. \tag{9}$$

The aim of the computations presented below is to determine the deposited film thickness $\lambda(\mathrm{Ca},\alpha)$, the pressure drop $\Delta p(\mathrm{Ca},\alpha)$ and the interface shape as functions of bubble speed Ca and wedge angle α.

C. Boundary-element method

We solve the problem formulated above using the boundary-element method, which is well suited to solving Stokes flows with free boundaries.[6,23] Using Green's theorem, an integral equation involving the velocity and stress on the surfaces of a domain is derived from (1),

$$C_{ki}u_i(\mathbf{x})+\int_\Gamma T_{ik}(\mathbf{x},\mathbf{y})u_i(\mathbf{y})\,dS(\mathbf{y})$$

$$=\int_\Gamma U_{ik}(\mathbf{x},\mathbf{y})\tau_i(\mathbf{y})dS(\mathbf{y}), \tag{10}$$

where $\mathbf{x}$ represents the position vector of a point on the surface Γ (as shown in Fig. 3), C_{ki} is a matrix which allows for a jump in normal stress, and $\boldsymbol{\tau}=\boldsymbol{\sigma}\cdot\mathbf{n}$ is the stress vector. The kernels U_{ik} and T_{ik} are given by

$$U_{ik}(\mathbf{x},\mathbf{y})=-\frac{1}{4\pi}\left(\delta_{ik}\log|\mathbf{x}-\mathbf{y}|-\frac{(x_i-y_i)(x_k-y_k)}{|\mathbf{x}-\mathbf{y}|^2}\right), \tag{11a}$$

$$T_{ik}(\mathbf{x},\mathbf{y})=-\frac{1}{\pi}\frac{(x_i-y_i)(x_j-y_j)(x_k-y_k)n_j(\mathbf{y})}{|\mathbf{x}-\mathbf{y}|^4}. \tag{11b}$$

The domain of integration shown in Fig. 3 is divided into 5 segments. Along each segment either a velocity or stress condition is applied in (10), enabling the unknown stress or velocity field on a given boundary to be uniquely determined. Along the bubble interface AB the stress condition (2) is enforced, and an iterative procedure described below is used to satisfy the kinematic boundary condition. On the channel wall CD the velocity (4) is specified, and (3) is imposed on the symmetry line EA. The domain is truncated along two arcs of circles (DE and BC), with radii $R_1=\mathrm{OD}$ and $R_2=\mathrm{OC}$, respectively, where $0<R_1<\cot\alpha<R_2$. R_1 is chosen to be sufficiently close to the vertex for the flow to be described by the self-similar solution given in Sec. II B. R_2 is chosen to be sufficiently large for the deposited film to be uniform and the flow unidirectional.

The surfaces are covered with quadratic elements, and the velocity and stress fields are approximated using locally quadratic polynomials over each element. A dense system of linear equations for the unknown stresses and velocities of the form $H\mathbf{w}=G\mathbf{t}$ is obtained, where $w_{2j-1}=u_j$, $w_{2j}=v_j$, $t_{2j-1}=\tau_{xj}$, $t_{2j}=\tau_{yj}$ for $j=1,\ldots,N$, N being the number of node points. With the exception of the diagonal entries of H, the entries of H and G are computed by evaluating the line integrals using either a regular Gaussian quadrature rule if the node point $\mathbf{x}$ is not on an element, or a logarithmic Gaussian quadrature rule if it is. The diagonal elements of H are determined from the off-diagonal elements by solving the system of equations analytically for a uniform velocity field. The size of matrix H is $4N\times 4N$ but G is a $6N\times 6N$ matrix that allows for jumps in the stress vector at the end-points of elements. This is important at corner points of the domain where the normal vector abruptly changes direction. Mixed velocity–stress conditions are applied at corner points as follows. On the node point on one side of a corner at $j=1$, say, (w_1,t_2) is specified whereas (t_1,w_2) is specified at the same node point on the other side of the corner, so that the unknowns are t_1 on the first side and t_2 on the second side. Here a vector of the form $(\cdot,\cdot)$ is associated with each node point, with prescribed horizontal and vertical components as described above. The resulting system of equations is solved using Gaussian elimination.

An iterative procedure is used to determine the shape of the bubble. For a given film thickness λ, a bubble shape is initially assumed so that the traction on the bubble surface can be computed. The boundary-element equations are then solved for the unknown velocities and stresses. Since the computed surface velocity does not satisfy the kinematic boundary condition, the initial shape is then perturbed, and the displacements normal to the initial node points on the

bubble surface are determined iteratively using Newton's method until the kinematic boundary condition at each node point is satisfied to a certain degree of accuracy.

There is an added complexity at the corner point D on the wall where the wedge flow is applied, since $t_1=\tau_{x1}$ and $t_2=\tau_{y1}$ are linear combinations of the shear stress and the pressure, given by

$$t_1^{(\mathrm{arc})}=\cos\,\alpha\,\sigma_{rr}-\sin\,\alpha\,\sigma_{r\theta}, \tag{12a}$$

$$t_2^{(\mathrm{wall})}=-\sin\,\alpha\,\sigma_{r\theta}-\cos\,\alpha\,\sigma_{\theta\theta}. \tag{12b}$$

Here the stress components are determined from the self-similar flow near the vertex (Sec. II B),

$$\sigma_{rr}=-p+\frac{2}{r^2}g_2'(\alpha),\quad \sigma_{\theta\theta}=-p-\frac{2}{r^2}g_2'(\alpha), \tag{13a}$$

$$\sigma_{r\theta}=\frac{1}{r}(g_1(\alpha)+g_1''(\alpha))-\frac{1}{r^2}g_2''(\alpha). \tag{13b}$$

Note that the constant p_k in the pressure [see (8)] is not known, but it can be determined in conjunction with the displacement field by ensuring that

$$t_1^{(\mathrm{wall})}+t_2^{(\mathrm{arc})}=\sin\,\alpha\,(\sigma_{rr}+\sigma_{\theta\theta}) \tag{14}$$

is satisfied.

To ensure that results were not dependent on the length of the computational domain, the boundary-integral equations were computed until the bubble interface near B in Fig. 3 was parallel to the wall. When necessary, the number of node points on the bubble surface was increased, in particular near the bubble tip, in order to capture accurately regions of high curvature. Because of the quadrature rules used to evaluate the boundary integrals, we were not able to consider cases with $\mathrm{Ca}<0.01$ for which the deposited film is very small. Between 100 and 300 node points were used, with α ranging from 1.5° to 45° and Ca between 0.02 to 10.

Computational results are presented in Sec. II F below. First, we describe two important limits that can be used to provide independent tests of our numerical results.

D. Solution for Ca≪1

When $\mathrm{Ca}\ll 1$, lubrication theory may be employed, following Bretherton[1] and numerous subsequent authors.[3,5–7] The deposited film thickness $\lambda\ll 1$, and to leading order the bubble tip forms a circular arc of radius $R=\cos\alpha/(1-\sin\alpha)$ which meets the wall tangentially. Let z measure distance along the upper wall from the contact point. Lubrication theory implies that the deposited film thickness $g(z)$ satisfies $\frac{1}{3}g^3p_z=\mathrm{Ca}(g-\lambda)$ where $p=-g_{zz}$. Rescaling, setting $g=\lambda G(\xi)$, with $z=\lambda\xi/(3\,\mathrm{Ca})^{1/3}$, the film thickness is governed by the Landau–Levich equation,[24]

$$G^3G_{\xi\xi\xi}=1-G,\quad G\to 1\quad \text{as}\quad \xi\to\infty \tag{15}$$

which appears in many coating-flow problems.[9,25,26] This equation has a unique solution for which $G\sim\frac{1}{2}G_2\xi^2+G_0$ as $\xi\to-\infty$, where $G_2\approx 0.64304$ and $G_0\approx 2.89964$. Since, away from the wall, the bubble has uniform curvature $1/R$, $g\sim z^2/(2R)$ where the film meets the bubble, which requires that

$$\lambda(\mathrm{Ca},\alpha)\sim(3\,\mathrm{Ca})^{2/3}G_2\frac{\cos\,\alpha}{1-\sin\,\alpha},\quad \text{for}\ \ \mathrm{Ca}\ll 1. \tag{16}$$

The first correction to the bubble radius curvature is $R-\lambda G_0$, so the leading-order pressure drop across the meniscus is

$$\Delta p(\mathrm{Ca},\alpha)\sim\frac{1-\sin\,\alpha}{\cos\,\alpha}(1+G_0G_2(3\,\mathrm{Ca})^{2/3}),\quad \text{for}\ \ \mathrm{Ca}\ll 1. \tag{17}$$

The next correction to Δp is the $O(\mathrm{Ca})$ contribution from the bulk flow ahead of the meniscus.

E. The limit α≪1

For small wedge angles the problem described in Sec. II A reduces to the Bretherton problem for a bubble in a parallel-sided channel.[1] The self-similar flow near the vertex described in Sec. II B is dominant along the majority of the channel ahead of the bubble tip [since neglected eigenfunctions decay like $r^{c/\alpha}$ for some constant $c=O(1)$ as $r\to 0$],[21,22] and [from (7)]

$$g_1\sim\mathrm{Ca}\frac{\theta}{2}\left(\frac{\theta^2}{\alpha^2}-1\right),\quad g_2\sim\lambda\,\mathrm{Ca}\frac{\theta}{2\alpha}\left(3-\frac{\theta^2}{\alpha^2}\right). \tag{18}$$

Thus for $\alpha\ll 1$, ψ_1 describes a parabolic velocity profile between walls moving with constant speed Ca; an adverse pressure gradient ensures zero net flux. ψ_2 denotes a parabolic velocity profile between stationary walls with flow rate $\lambda\mathrm{Ca}$ driven by a favorable pressure gradient. The pressure distribution along the axis of symmetry is approximately

$$p\approx-\frac{3\,\mathrm{Ca}}{\alpha(1-X)}+\frac{3\lambda\,\mathrm{Ca}}{2\alpha(1-X)^2}+p_k, \tag{19}$$

where $X=1-r\alpha$ measures distance from the meniscus tip over a long $O(1/\alpha)$ lengthscale. Thus towards the bubble tip, as $X\to 0+$,

$$p\approx p_k+\frac{3\,\mathrm{Ca}}{2\alpha}(\lambda-2)+\frac{3\,\mathrm{Ca}}{\alpha}(\lambda-1)X+O(X^2), \tag{20}$$

implying that the pressure distribution in the liquid far from the vertex, but a few channel widths upstream of the bubble tip, has a mean value plus an approximately linear gradient. This is exactly as one would expect for bubble motion in a parallel-sided channel with a Poiseuille flow ahead of the bubble. In this limit,

$$\Delta p\approx-\left[p_k+\frac{3\,\mathrm{Ca}}{2\alpha}(\lambda-2)\right], \tag{21}$$

so that for fixed Ca, p_k is singular as $\alpha\to 0$ but Δp remains bounded.

We anticipate that as $\alpha\to 0$, $\lambda\sim\lambda_0(\mathrm{Ca})$ and $\Delta p\sim\Delta p_0(\mathrm{Ca})$, where λ_0 and Δp_0 are previously computed solutions of the Bretherton problem (e.g., Refs. 4, 6), regres-

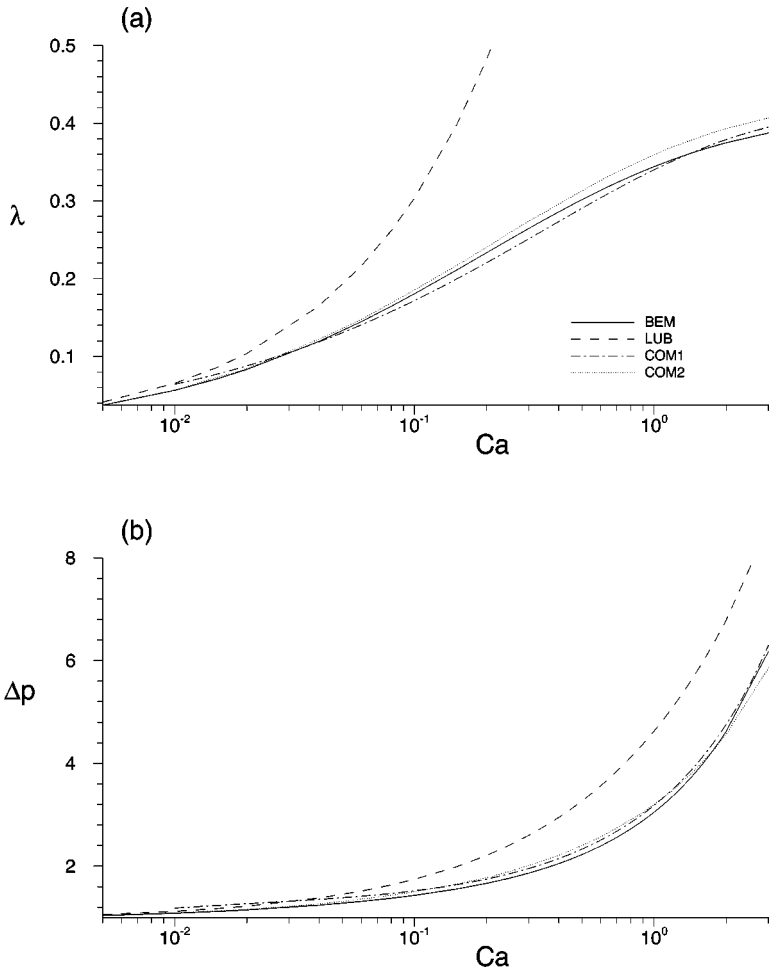

FIG. 4. Comparisons between boundary-element results (solid, BEM), low-Ca asymptotics [(16), (17), dashed, LUB] and the composite approximation (22) based on data from Ref. 4 (dot–dashed, COM1) and the regression formula of Ref. 6 (dotted, COM2): (a) λ and (b) Δp vs Ca for $\alpha=\pi/60$.

sion formulas for which are given in the Appendix. Motivated by (16), (17), which show how the film thickness and pressure drop scale on the radius of curvature of the bubble tip as α increases, we define the composite approximation,

$$\hat{\lambda}=\lambda_0(\mathrm{Ca})\frac{\cos\alpha}{1-\sin\alpha},\quad \Delta\hat{p}=\Delta p_0(\mathrm{Ca})\frac{1-\sin\alpha}{\cos\alpha},\quad (22)$$

which we use below in validating numerical results. Since $\hat{\lambda}-\lambda_0$ and $\Delta\hat{p}-\Delta p_0$ are both $O(\alpha)$ as $\alpha\to 0$, we may use (22) to verify computational results for either small Ca or small α.

F. Results

In order to assess the accuracy of the results obtained from the boundary-element method, comparisons are first made with results for small wedge angles (Fig. 4) and low Ca (Fig. 5). In Fig. 4, the film thickness and the pressure drop are plotted versus Ca for $\alpha=\pi/60$. As expected from the Bretherton problem, λ increases with Ca, agreeing with the two-thirds power law (16) at very small Ca and leveling off at large Ca. Also as expected, the pressure drop increases with increasing Ca (we expect $\Delta p\propto \mathrm{Ca}$ for $\mathrm{Ca}\gg 1$, making the dimensional pressure drop independent of γ in this limit). The composite approximation given by (22), based on two independent sets of numerical data,[4,6] works well over the whole range of Ca for these low values of α.

The effect of varying wedge angle for $\mathrm{Ca}=0.02$ is examined in Fig. 5. As anticipated from (22), increasing α leads to an increase in λ and a decrease in Δp. The fall in pressure drop arises because, at low Ca, capillary effects dominate Δp, and increasing α reduces the bubble tip curvature and hence Δp. There is good agreement between boundary-element data and the composite approximation (22) based on Reinelt's data[4] for the film thickness at small α, although the boundary-element data deviate from the formula as the wedge angle increases, indicating the first nontrivial effect of channel taper. As suggested in Fig. 4, lubrication theory provides a poor approximation of film thickness because $\mathrm{Ca}>0.01$.

The effects of taper on film thickness and pressure drop are illustrated in Fig. 6, where λ and Δp are plotted versus α/π for fixed $\mathrm{Ca}\in[0.02,10]$. This figure shows the most striking prediction of these computations, namely that whereas λ increases with α for low Ca [as seen already in Fig. 5, and as indicated in (16)], for large Ca (e.g., $\mathrm{Ca}=10$) the deposited film thickness diminishes with an increasing wedge angle (for α sufficiently large). The existence of a maximum in the λ vs α curves is not anticipated from any approximate analysis, and arises through the inherent nonlinearity in the problem. The value of α at which this maximum film thickness occurs decreases with increasing Ca. The closer spacing of the large-Ca curves as α increases

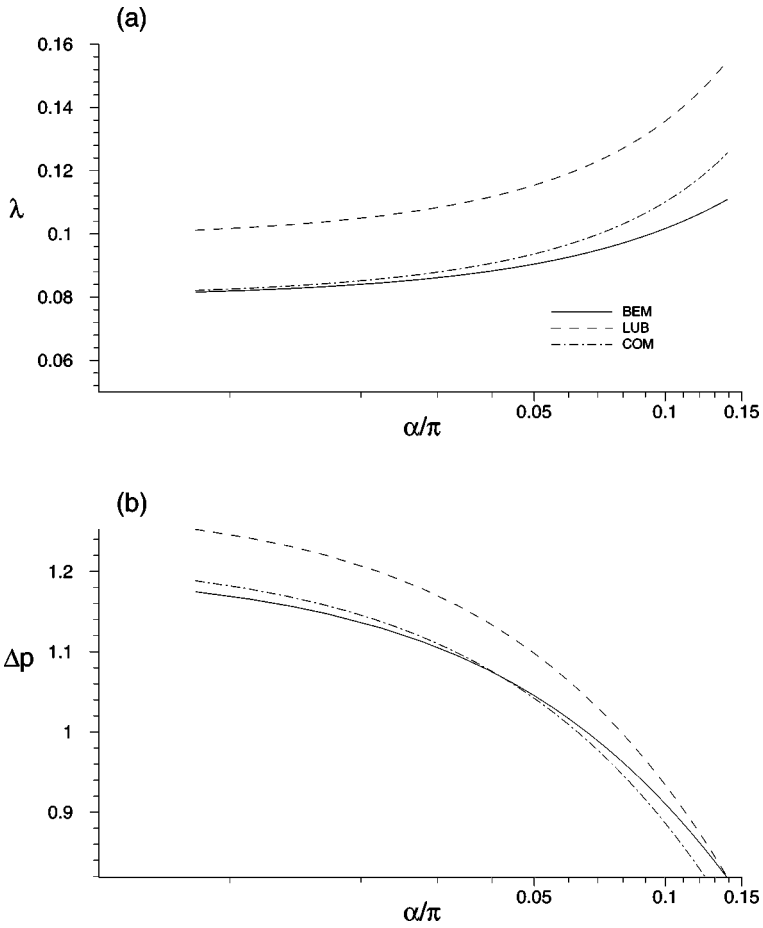

FIG. 5. Comparisons between boundary element results (solid, BEM), low-Ca asymptotics [(16), (17), dashed, LUB] and the composite approximation (22) based on data from Ref. 4 (dot–dashed, COM): (a) λ and (b) Δp vs α/π for Ca$=0.02$.

in Fig. 6 suggests that λ, which always increases with Ca for fixed α, asymptotes to its final value more quickly at large α than at small α. A qualitative explanation for this behavior is that increasing α reduces the curvature of the bubble tip, lessening the importance of capillary effects, so that viscous-dominated (large-Ca) behavior arises more readily. This effect is not captured in the composite approximation (22), since Ca appears independently of α in (22). Similarly, while the pressure drop falls with increasing α at low Ca, Fig. 6(b) shows that it can increase with α at sufficiently large Ca. Diminishing film thicknesses with Ca large and α increasing may lead to elevated viscous pressure losses that appear in Δp.

The influence of Ca and α on bubble shape is shown in Figs. 7 and 8. Note that, due to symmetry, only the upper half of the wedge is shown, and cot α has been subtracted from the x coordinate so that bubble tip is at the origin. At small wedge angles [Fig. 7(a)], the deposited film thickness and the bubble tip curvature increase with Ca, until Ca is large enough for viscous effects to dominate over surface tension effects and, as in parallel-sided channel problem, the shape becomes insensitive to the value of Ca. At larger wedge angles [Fig. 7(b)], the bubble approaches its large-Ca shape at a lower Ca, consistent with Fig. 6(a). For Ca$=0.1$ [Fig. 8(a)], the film thickness behind the advancing bubble tip clearly increases with wedge angle, whereas this is not so for Ca$=1$ [Fig. 8(b)], which again is consistent with Fig. 6(a).

III. UNSTEADY SELF-SIMILAR MOTION

A. The model

Consider now a semi-infinite bubble drawn at constant speed $\mathcal{U}$ into a wedge, the walls of which subtend an angle 2α and are stationary [Fig. 1(b)]. Symmetry about the midplane is assumed, and again the pressure in the bubble is taken to be zero. We assume the existence of a sink at the vertex such that at time $t \leqslant t_0$, the bubble tip lies a distance $\mathcal{U}(t_0-t)$ from the wedge vertex.

We seek a similarity solution of the governing Stokes equations, parametrized by Ca$=\mu\mathcal{U}/\gamma$ and the wedge angle α. We scale lengths on $a(t)=\mathcal{U}(t_0-t)\tan\alpha$ (the vertical channel width at the bubble tip), speeds on $\mathcal{U}\tan\alpha$, and pressure on the viscous scale $\mu\mathcal{U}\tan\alpha/a=\mu/(t_0-t)$. The governing equations in the fluid are (1), with

$$\mathbf{u}=\mathbf{0}, \quad \text{on } y=x\tan\alpha. \tag{23}$$

The symmetry condition (3) holds along $y=0$, $0<x \leqslant \cot\alpha$, and the stress condition (2a) holds along the bubble interface, which lies at $y=h(x)$ in $x \geqslant \cot\alpha$ (see Fig. 9). The only time-derivative in the problem appears in the kinematic boundary condition ($h^*_{t^*}+u^*h^*_{x^*}=v^*$ in dimensional variables), so that in dimensionless variables this becomes

$$-h+xh_x+uh_x=v, \quad \text{on } y=h(x). \tag{24}$$

The dimensional flux $\mathcal{U}^2(t_0-t)\tan\alpha\, Q(x)$, where

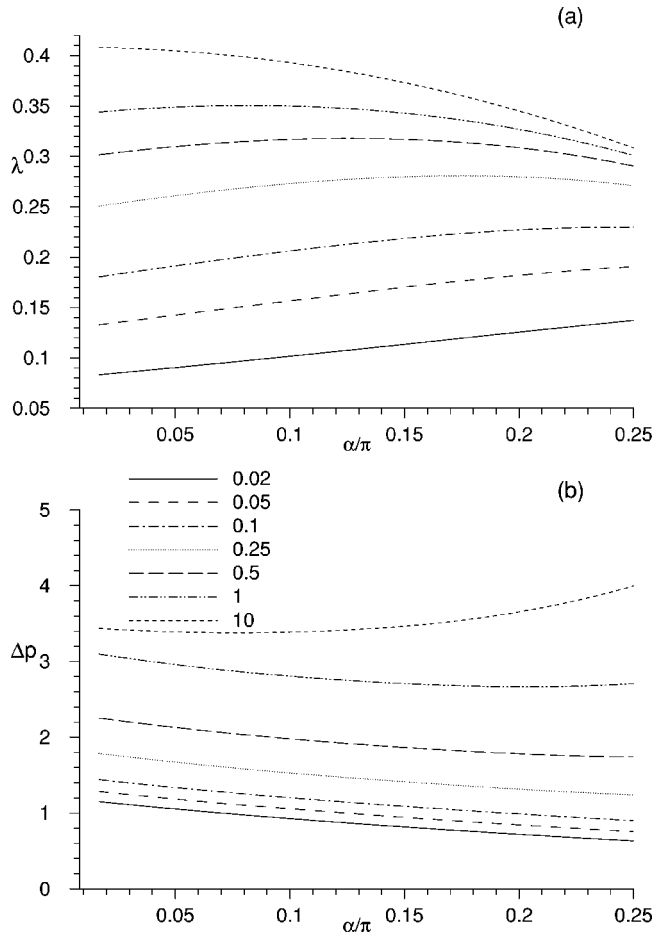

FIG. 6. (a) λ and (b) Δp vs α/π for values of Ca between 0.02 (solid) and 10 (dashed). Δp for Ca=10 has been reduced by a factor of 5.

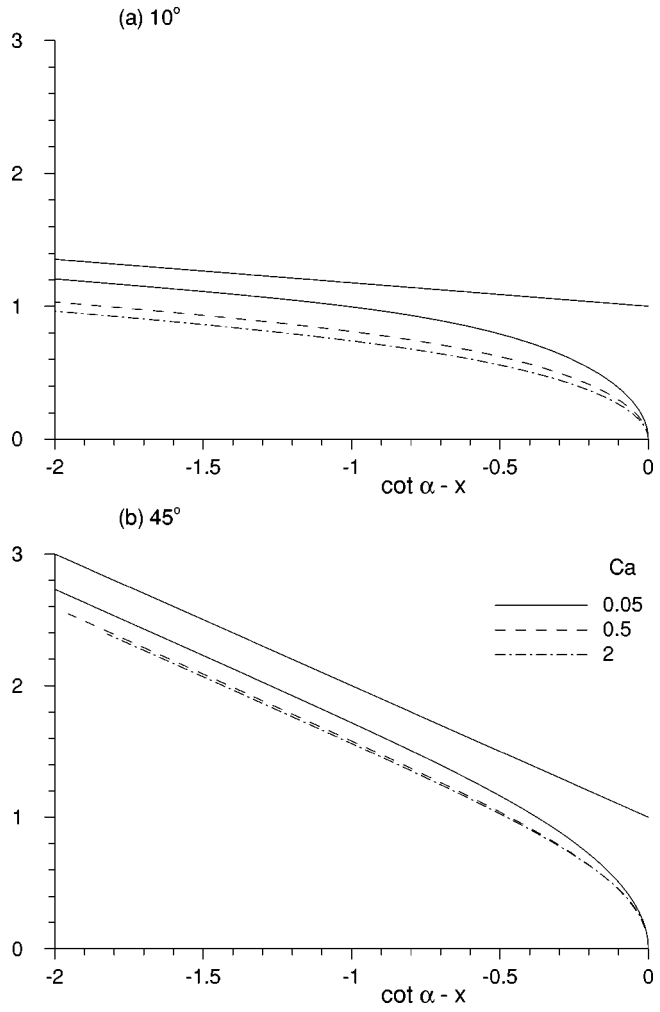

FIG. 7. Curves show bubble width $y=h$ versus axial distance x for various Ca (only the upper half of the bubble shape is shown due to symmetry) for wedge angles (a) $\alpha=10°$ and (b) $\alpha=45°$. In order to fix the bubble tip at the origin, cot α is subtracted from x (see Fig. 2). The solid line passing through (0,1) denotes the upper channel wall; —, Ca=0.05; ---, Ca=0.5; -·-, Ca =2.

$$Q=\int_{h(x)}^{x\tan\alpha} u\,dy \tag{25}$$

(defining $h\equiv 0$ in $0<x<\cot\alpha$), therefore satisfies

$$Q_x=-h+xh_x. \tag{26}$$

For $x\to\infty$, $h\sim\beta x$ where $0<\beta<\alpha$, so that the film deposited on the channel walls is wedge-shaped (see Fig. 9), consistent with the assumption of self-similarity. Thus $Q\to 0$ as $x\to\infty$, since here the deposited fluid is stationary with respect to the channel walls. Likewise in $0<x<\cot\alpha$, where $h=0$, $Q=S$ for some constant $S<0$ which represents the strength of the sink at the vertex of the channel. Integrating (26), we therefore have

$$S=\int_{\cot\alpha}^{\infty}(h-xh_x)\,dx. \tag{27}$$

The flow near the vertex of the wedge now has a single component, with streamfunction $\psi\sim g_2(\theta)$ as $r\to 0$, where g_2 is given by (7b). The local pressure distribution is $p\sim p_2(r,\theta)+p_k$ [as in (8)], and the pressure drop across the bubble tip is therefore defined as

$$\Delta p=-[p_2(\cot\alpha,0)+p_k]. \tag{28}$$

The aim of the computations presented below is to determine the angle subtended by the deposited fluid wedge ($\alpha-\beta$; see Fig. 9) and the pressure drop Δp as functions of Ca and α. A boundary-element code was developed following closely the scheme outlined in Sec. II C, although it was only possible to cover a reduced range of α and Ca with acceptable accuracy, for reasons outlined below. Again, we consider some important limiting cases before presenting numerical results in Sec. III D below.

B. Solution for Ca≪1

It is most convenient to derive the low-Ca solution in dimensional variables, denoted with asterisks. As in Sec. II D, at leading order the bubble tip forms a meniscus which is an arc of a circle of radius,

$$R^*=\sin\alpha\,\mathcal{U}(t_0-t)/(1-\sin\alpha), \tag{29}$$

which meets the wall at

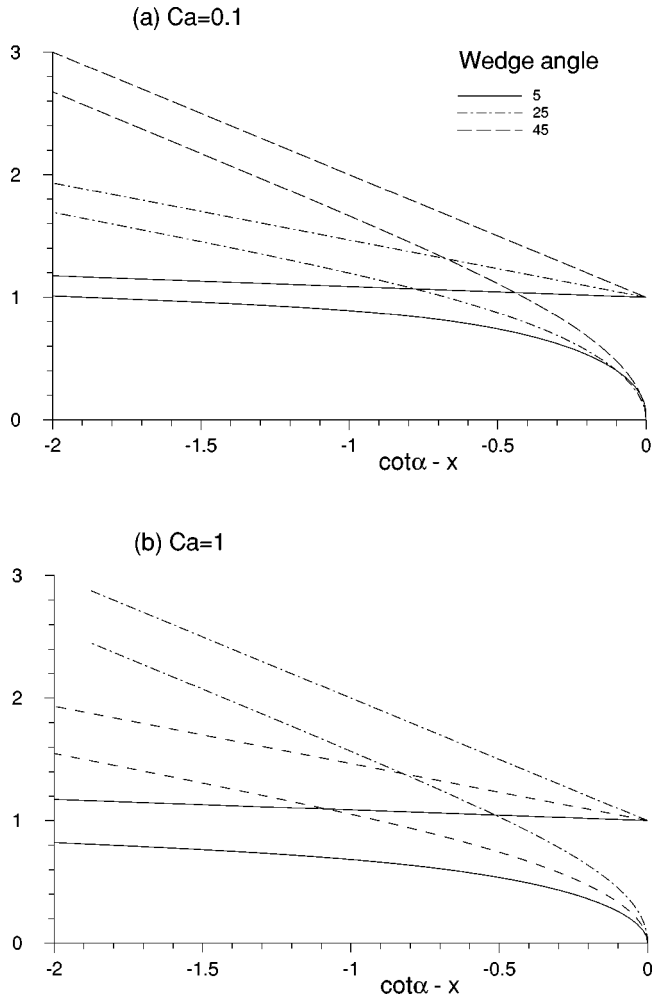

FIG. 8. Bubble width $y=h$ is plotted against axial distance for various wedge angles with (a) Ca=0.1 and (b) Ca=1; — $\alpha=5°$; -·- $\alpha=25°$; - - - $\alpha=45°$. Each straight line through (0,1) shows the corresponding channel boundary.

$$(x^*,y^*)=\mathcal{U}(t_0-t)\frac{(1+\sin\alpha)}{\cos\alpha}(\cos\alpha,\sin\alpha). \tag{30}$$

The speed of the contact point relative to the wall is therefore $\mathcal{U}(1+\sin\alpha)/\cos\alpha$, so that the effective capillary number is

$$\hat{\mathrm{Ca}}=\mathrm{Ca}(1+\sin\alpha)/\cos\alpha. \tag{31}$$

The thickness of the deposited film is therefore [by analogy to (16)]

$$\lambda^*=(3\hat{\mathrm{Ca}})^{2/3}G_2\frac{\sin\alpha\,\mathcal{U}(t_0-t)}{1-\sin\alpha}, \tag{32}$$

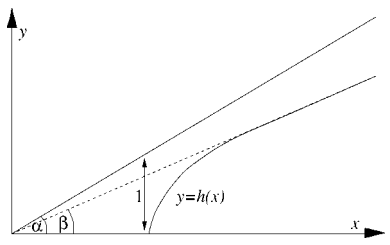

FIG. 9. A bubble moving into a planar wedge.

where G_2 is given in Sec. II D. Since the distance from the vertex of the wedge to the contact point is $R^*/\tan\alpha$, it follows that $\alpha-\beta\sim\lambda^*\tan\alpha/R^*$, and so

$$\alpha-\beta\sim(3\hat{\mathrm{Ca}})^{2/3}G_2\tan\alpha, \quad \text{for Ca}\ll 1. \tag{33}$$

Correspondingly, the dimensionless pressure drop across the meniscus is

$$\Delta p\sim\frac{1}{\mathrm{Ca}}\frac{(1-\sin\alpha)}{\sin\alpha}[1+(3\hat{\mathrm{Ca}})^{2/3}G_0G_2], \quad \text{for Ca}\ll 1. \tag{34}$$

C. The limit $\alpha\to 0$

If the bubble tip is a dimensional distance $\mathcal{U}(t_0-t)$ from the vertex, then the channel width near the bubble tip is $a(t)\sim\alpha\mathcal{U}(t_0-t)$ for $\alpha\ll 1$. Since the channel is almost parallel-sided here, the dimensional thickness of the deposited film is $\lambda_0(\mathrm{Ca})a(t)$, and the dimensional pressure drop across the bubble is $\gamma\Delta p_0(\mathrm{Ca})/a(t)$, where once again λ_0 and Δp_0 are the film thickness and pressure drop of the parallel-sided problem (as in Sec. II E). The angle subtended at the vertex by the deposited film is therefore $\lambda_0 a/\mathcal{U}(t_0-t)$, so that the wedge angle and the dimensionless pressure drop are

$$\alpha-\beta\sim\alpha\lambda_0(\mathrm{Ca}), \quad \Delta p\sim\frac{\Delta p_0(\mathrm{Ca})}{\alpha\mathrm{Ca}} \quad \text{for} \quad \alpha\ll 1. \tag{35}$$

Once again we can define a composite approximation that reduces to (33), (34) and (35) in the appropriate limits:

$$\alpha-\hat{\beta}=\lambda_0(\hat{\mathrm{Ca}})\tan\alpha, \quad \Delta\hat{p}=\frac{(1-\sin\alpha)}{\mathrm{Ca}\sin\alpha}\Delta p_0(\hat{\mathrm{Ca}}), \tag{36}$$

where $\hat{\mathrm{Ca}}$ is given by (31).

D. Results

The range of boundary-element results presented below is smaller than those in Sec. II F, because the bubble tip curvature increases rapidly with α and Ca while the interfacial curvature decreases rapidly with distance from the tip. These curvatures could not be accurately resolved using the cubic spline polynomial approximation for the bubble shape that was used in the boundary-element algorithm. However, sufficient coverage of parameter space is provided to give a reasonably clear picture of the important behavior.

As before, we first compare numerical predictions of $\alpha-\beta$ and Δp against approximations for low Ca and low α given in (33)–(36). The effect of Ca on the deposited film thickness is shown in Figs. 10(a) and 10(b), indicating that the angle $\alpha-\beta$ subtended by the deposited film, as a fraction of the total wedge angle α, increases with Ca for fixed α. For $\alpha=5°$, numerical results agree closely with the composite solution based on (36) using Reinelt's data,[4] diverging slightly as Ca increases. The composite approximation naturally converges with the lubrication theory approximation (33) at small Ca, and as before (33) significantly overpredicts the film thickness as Ca increases. The film thickness for $\alpha=20°$ [Fig. 10(b)] is uniformly thicker than the correspond-

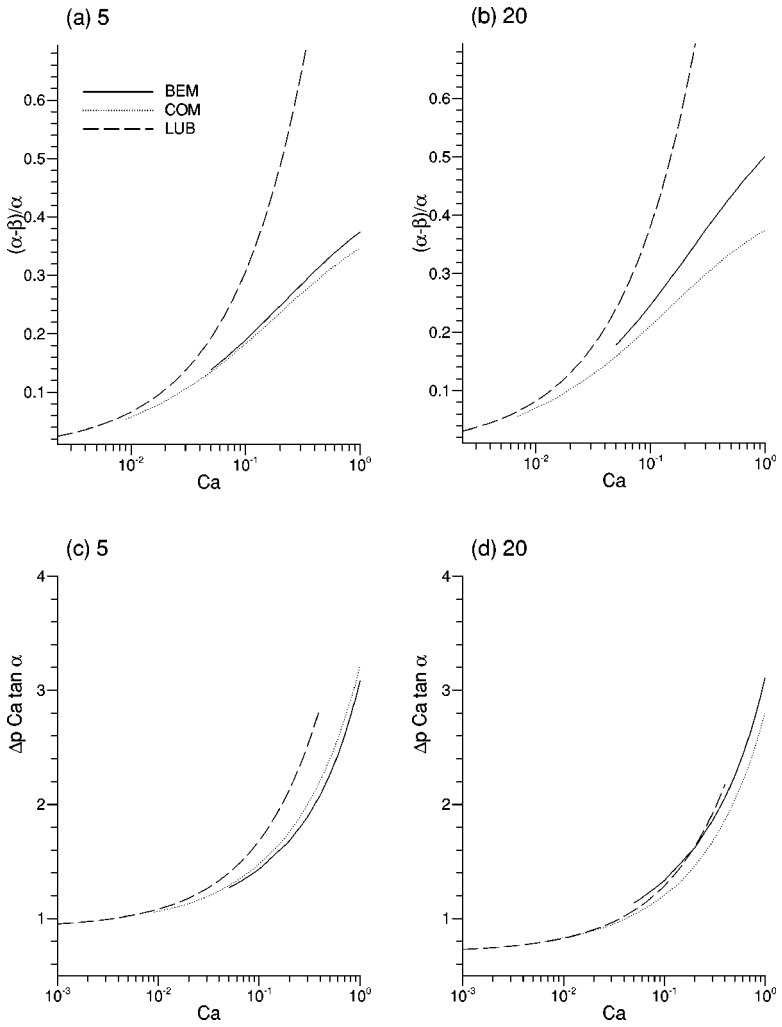

FIG. 10. The angle subtended by the deposited film, $(\alpha-\beta)/\alpha$ for (a) $\alpha=5°$ and (b)$\alpha=20°$, and pressure drop, Δp Ca tan α, versus Ca for (c) $\alpha=5°$ and (d) $\alpha=20°$, using the boundary-element method (BEM), the composite approximation (36, COM) and lubrication theory (33, 34, LUB).

ing thickness for $\alpha=5°$ for any Ca, and the composite approximation and numerical solution diverge at a lower Ca, indicating that the nontrivial effects of taper appear at lower Ca for larger α.

To allow a comparison with the results in Sec. II F, we plot the rescaled pressure drop ΔpCa tan α (which is equivalent to scaling the dimensional pressure drop on the capillary scale γ/a) vs Ca for $\alpha=5°$ and $\alpha=20°$ in Figs. 10(c) and 10(d). As in the steady problem, the pressure drop is an increasing function of Ca for fixed α. For $\alpha=5°$, the numerical solution agrees well with (36b) over a wide range of Ca, and it converges with (34) for low Ca; again the agreement with the composite solution is less good (as expected) for $\alpha=20°$.

The effect of varying the wedge angle on $(\alpha-\beta)/\alpha$, on Δp Ca tan α and on S tan α is shown in Fig. 11. For a given Ca, increasing the wedge angle in the range shown in Fig. 11(a) causes a modest increase in the film thickness angle at small α, and a more pronounced increase at moderate α, consistent with the angular dependency of $\alpha-\beta$ given by (33). We found no evidence of the nonmonotonic behavior of film thickness that arises in the steady problem [Fig. 6(a)], although we were only able to survey a narrower range of parameter space with acceptable numerical accuracy. The results suggest that the film thickness becomes increasingly sensitive to Ca as α increases, unlike the steady problem [Fig. 6(a)]. The corresponding rescaled pressure drop [Fig. 11(b)] decreases slightly with α for low Ca, and shows evidence of weakly nonmonotonic behavior at larger Ca, but overall is largely insensitive to α for the parameters investigated. These results mask the strong dependence of the dimensional pressure drop on α through the scaling factor tan α. The quantity S tan α, proportional to the sink strength S, decreases slightly with wedge angle [Fig. 11(c)], and for fixed α decreases with Ca. However, because the dimensional flux strength contains a factor $\mathcal{U}^2$, the dimensional sink strength actually increases in magnitude with Ca for fixed α.

The effect of varying Ca and α on bubble shape is shown in Fig. 12. For a wedge angle of 20°, the curvature of the bubble tip and consequently the subtended wedge angle far from the tip increase with Ca [Fig. 12(a)], which is expected from both the steady-state results in section II and the Bretherton problem. However, the film thickens very substantially as Ca increases, showing much stronger variation with Ca than in Fig. 7. In Fig. 12(b), the effect of α on bubble shape is shown for Ca$=0.1$. Again we see a significantly greater increase in film thickness with increasing wedge angle than in Fig. 8, but much less change in the curvature of the bubble tip.

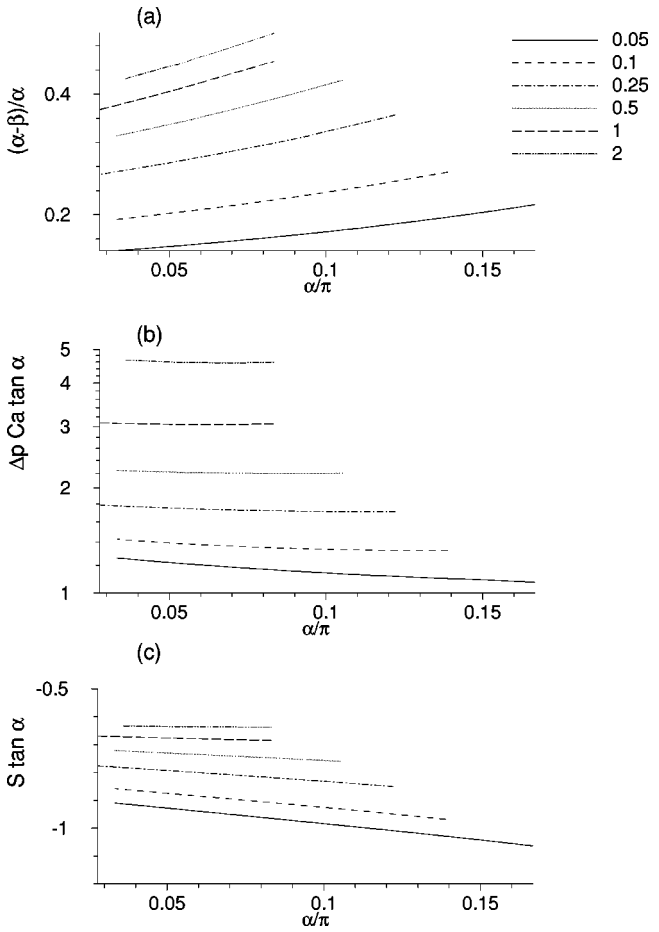

FIG. 11. (a) The angle subtended by the deposited film, $(\alpha-\beta)/\alpha$, (b) pressure drop, Δp Ca tan α, and (c) sink strength, S tan α, versus α/π for several Ca using the boundary element method.

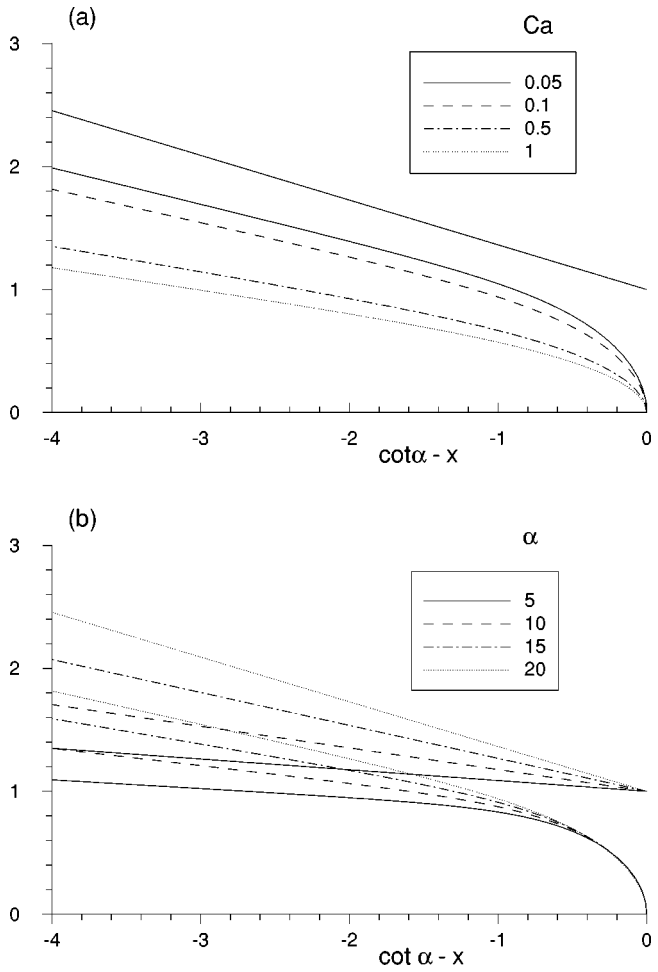

FIG. 12. (a) The effect of Ca on bubble shape for $\alpha=20°$. (b) The effect of wedge angle on bubble shape for Ca$=0.1$.

IV. DISCUSSION

We have considered the two fundamental Stokes flows illustrated in Fig. 1, in which a semi-infinite bubble advances into a two-dimensional channel, in order to examine the effects of channel taper on the thickness of the film deposited on the channel walls and on the pressure drop across the bubble tip. In each case the flows are parametrized by the taper angle α and a capillary number Ca. In the steady problem [Fig. 1(a)], the deposited film thickness increases with taper angle at low Ca, in line with predictions of lubrication theory, but at large Ca the film thickness falls quite significantly as α increases [Fig. 6(a)]. Similar nonmonotonic behavior is seen for the pressure drop [Fig. 6(b)]. The parameter regime in which this behavior occurs suggests that it is a predominantly viscous, rather than capillary, phenomenon. The underlying mechanism is hard to explain in simple physical terms, however, because quite different behavior is observed in the unsteady problem [Fig. 1(b)]. Here, the deposited film thickness (measured as a fraction of the total wedge angle subtended by the wedge-shaped film) always increases monotonically with α and Ca, at least for the range of parameter values that we investigated numerically [Fig. 11(a)], and (perhaps for largely geometric reasons) the thickness is much more sensitive to changes in α and Ca in the unsteady problem. For the steady problem, the primary effect of taper appears to be to increase the effective capillary number of the flow by reducing the curvature of the bubble tip (Fig. 8), so increasing the relative importance of viscous to capillary forces. This effect is not reflected in the unsteady problem for the parameter values that we investigated. An important message of the present study is therefore that results for steady free-surface Stokes flows cannot be reliably extrapolated to analogous unsteady problems.

Our original motivation for this study came from an investigation of the reopening of flooded and collapsed lung airways.[12] We modeled this process as a pair of wet membranes being peeled apart by an advancing bubble. In developing a rational asymptotic description of this physical model,[20] in the limit of large membrane tension (ensuring uniformly small membrane slopes), it is necessary to have available the results of the ''Bretherton'' problem at arbitrary Ca, plus the leading-order effects of weak taper $\alpha \ll 1$. In the present study we provide this important correction, through the function

$$\lambda_1(\mathrm{Ca}) = \frac{\partial \lambda}{\partial \alpha}(0,\mathrm{Ca}), \tag{37}$$

for which an approximate regression formula is provided in

the Appendix. Note from (22) that $\lambda_1 \sim \lambda_0(\mathrm{Ca}) > 0$ for $\alpha \ll 1$. We find numerically that $\lambda_1 > 0$ for $\mathrm{Ca} \lesssim 10.74$, and is negative for larger Ca. While this correction improves the accuracy of the asymptotic reopening model where membrane slopes are small, the asymptotic model significantly underestimates the bubble pressure required to reopen a collapsed channel at large Ca where slopes start to grow. Figure 6(a) provides one obvious explanation for this. At large Ca, extrapolation of the λ curves from their gradients at $\alpha = 0$ significantly overestimates the deposited film thickness, which consequently leads to erroneously high predictions of bubble pressure in the reopening problem. The results in this airway reopening study therefore suggest that the effect exhibited in Fig. 6(a) at large α and Ca contributes directly to an increase the pressure required to reinflate a collapsed lung airway.

The two problems examined here belong to a wider class of problems involving bubbles in tapered channels. We could naturally consider a long, finite-length bubble entering a converging or diverging channel: by treating the nose of a bubble in a converging channel, we have considered here only one out of four canonical configurations. Such problems find direct application to viscous fingering problems. Reinelt,[18] for example, computed the corrections to film thickness and pressure drop due to channel taper for $\mathrm{Ca} \ll 1$ when investigating instabilities of a viscous liquid partially filling the gap between two eccentric rotating cylinders. Our results provide an extension of these results (for a meniscus entering a converging channel) to finite Ca and finite taper angles, that could be exploited to extend stability analyses of fingering problems. Present analyses include that of Ruschak,[8] for example, who gives the boundary of stability in the steady problem in (α,Ca)-space, showing that the effects of taper are only weakly stabilizing to fingering instabilities for systems that are laterally unconfined. Various similarity solutions for analogous two-dimensional (2-D) potential (Hele–Shaw) flows between parallel plates in convergent or divergent wedge-shaped domains have also been explored in the context of the selection problem in the limit of small surface tension (e.g., Refs. 27–30). No selection problem arises when viscous effects are present, although the present results can now be used to provide improved boundary conditions for Hele–Shaw flows between nonparallel plates.

ACKNOWLEDGMENTS

During the course of this work, D.H. was supported by EPSRC Grant No. GR/M84572, and wishes to acknowledge support by Professor D. P. Gaver III, Tulane University, through National Science Foundation (NSF) Grant No. BCS-9978605.

APPENDIX: REGRESSION FORMULAS

The following are regression formulas for film thickness in a parallel-sided channel[6] for $\mathrm{Ca} > 0.01$,

$$\lambda_0(\mathrm{Ca}) \approx 0.417(1 - \exp[-1.69\ \mathrm{Ca}^{0.5025}]),$$

pressure drop in a parallel-sided channel[20]

$$\log_{10}(\Delta p/\mathrm{Ca}) \approx -2.00858 + 8.92426 \times \exp[-0.038332\,(Z+5)^{2.17398}] + 0.898217\,Z, \quad \text{(A1)}$$

where $Z \equiv \log_{10} \mathrm{Ca}$, and the leading-order effect of taper on film thickness (37),

$$\lambda_1 \approx 0.0769 - 0.04119z - 4.63\times10^{-3}z^2 + 4.46\times10^{-3}z^3 + 2.47442\times10^{-4}z^4 - 2.12954\times10^{-4}z^5 - 2.51264\times10^{-5}z^6, \quad \text{(A2)}$$

where $z \equiv \log \mathrm{Ca}$.

[1] F. P. Bretherton, "The motion of long bubbles in tubes," J. Fluid Mech. **10**, 166 (1961).
[2] K. J. Ruschak, "Boundary-conditions at a liquid-air interface in lubrication flows," J. Fluid Mech. **119**, 107 (1982).
[3] D. A. Reinelt and P. G. Saffman, "The penetration of a finger into a viscous fluid in a channel and tube," SIAM (Soc. Ind. Appl. Math.) J. Sci. Stat. Comput. **6**, 352 (1985).
[4] D. A. Reinelt, "Interface conditions for two-phase displacement in Hele–Shaw cells," J. Fluid Mech. **183**, 219 (1987).
[5] C. W. Park and G. M. Homsy, "Two-phase displacement in Hele–Shaw cells: Theory," J. Fluid Mech. **139**, 291 (1984).
[6] D. Halpern and D. P. Gaver III, "Boundary-element analysis of the time-dependent motion of a semi-infinite bubble in a channel," J. Comput. Phys. **115**, 366 (1994).
[7] M. D. Giavedoni and F. A. Saita, "The axisymmetric and plane cases of a gas phase steadily displacing a Newtonian liquid—A simultaneous solution of the governing equations," Phys. Fluids **9**, 2420 (1997).
[8] K. J. Ruschak, "Coating flows," Annu. Rev. Fluid Mech. **17**, 65 (1985).
[9] E. O. Tuck and L. W. Schwartz, "A numerical and asymptotic study of some third-order ordinary differential equations relevant to draining and coating flows," SIAM Rev. **32**, 453 (1990).
[10] W. L. Olbricht, "Pore-scale prototypes of multiphase flow in porous media," Annu. Rev. Fluid Mech. **28**, 187 (1996).
[11] D. Halpern and T. W. Secomb, "The squeezing of red blood cells through capillaries with near-minimal diameters," J. Fluid Mech. **203**, 381 (1989).
[12] D. P. Gaver III, D. Halpern, O. E. Jensen, and J. B. Grotberg, "The steady motion of a semi-infinite bubble through a flexible-walled channel," J. Fluid Mech. **319**, 25 (1996).
[13] P. H. Gaskell, M. D. Savage, J. L. Summers, and H. M. Thompson, "Modelling and analysis of meniscus roll coating," J. Fluid Mech. **298**, 113 (1995).
[14] A. D. McEwan and G. I. Taylor, "The peeling of a flexible strip attached by a viscous adhesive," J. Fluid Mech. **26**, 1 (1966).
[15] D. J. Coyle, C. W. Macosko, and L. W. Scriven, "Film-splitting flows in forward roll coating," J. Fluid Mech. **171**, 183 (1986).
[16] J. R. A. Pearson, "The instability of uniform viscous flow under rollers and spreaders," J. Fluid Mech. **7**, 481 (1960).
[17] E. Pitts and J. Greiller, "The flow of thin liquid films between rollers," J. Fluid Mech. **11**, 33 (1961).
[18] D. A. Reinelt, "The primary and inverse instabilities of directional viscous fingering," J. Fluid Mech. **285**, 303 (1995).
[19] T. W. Secomb and R. Hsu, "Motion of red blood cells in capillaries with variable cross-sections," ASME J. Biomech. Eng. **118**, 538 (1996).
[20] O. E. Jensen, M. K. Horsburgh, D. Halpern, and D. P. Gaver III, "The steady propagation of a bubble in a flexible-walled channel: Asymptotic and computational models," Phys. Fluids **14**, 443 (2002).
[21] H. K. Moffatt, "Viscous and resistive eddies near a sharp corner," J. Fluid Mech. **18**, 1 (1964).
[22] H. K. Moffatt and B. R. Duffy, "Local similarity solutions and their limitations," J. Fluid Mech. **96**, 299 (1980).
[23] C. Pozrikidis, *Boundary Integral and Singularity Methods for Linearized Viscous Flow* (Cambridge University Press, Cambridge, 1992).
[24] L. D. Landau and B. Levich, "Dragging of a liquid by a moving plate," Acta Physicochim. URSS **17**, 42 (1942).

[25]S. D. R. Wilson, ''The drag-out problem in film coating theory,'' J. Eng. Math. **16**, 209 (1982).
[26]O. E. Jensen, ''Draining collars and lenses in liquid-lined vertical tubes,'' J. Colloid Interface Sci. **221**, 38 (2000).
[27]H. Thomé, M. Rabaud, V. Hakim, and Y. Couder, ''The Saffman–Taylor instability: From the linear to the circular geometry,'' Phys. Fluids A **1**, 224 (1989).
[28]Y. Tu, ''Saffman-Taylor problem in sector geometry: Solution and selection,'' Phys. Rev. A **44**, 1203 (1991).
[29]M. Ben Amar, V. Hakim, M. Mashall, and Y. Couder, ''Self-dilating viscous fingers in wedge-shaped Hele–Shaw cells,'' Phys. Fluids A **3**, 1687 (1991).
[30]R. Combescot, ''Saffman–Taylor fingers in the sector geometry,'' Phys. Rev. A **45**, 873 (1992).